International Journal of Heat and Mass Transfer 52 (2009) 316–327

Contents lists available at ScienceDirect

International Journal of Heat and Mass Transfer

journal homepage: www.elsevier.com/locate/ijhmt

Fluid dynamics and oxygen transport in a micro-bioreactor with a tissue engineering scaffold

Peng Yu [a,*], Thong See Lee [a], Yan Zeng [a], Hong Tong Low [a,b]

[a] Department of Mechanical Engineering, National University of Singapore, 9 Engineering Drive 1, Singapore 117576, Singapore
[b] Division of Bioengineering, National University of Singapore, Singapore 117576, Singapore

ARTICLE INFO

Article history:
Received 18 September 2007
Received in revised form 12 June 2008
Available online 17 August 2008

Keywords:
Oxygen transport
Tissue engineering scaffold
Micro-bioreactor
Porous–fluid interface
Swirling flow
Interface coupling

ABSTRACT

The flow environment in the micro-bioreactor with a tissue engineering scaffold was numerically modeled. The finite volume method based on multi-block grid was applied to simulate the coupled flow and oxygen transport in both porous medium and homogenous fluid regions. At porous–fluid interface, a stress jump condition that includes both viscous and inertial effects was imposed. A parametric study was performed to investigate the effects of Reynolds, Darcy, and Damkohler numbers on the flow and oxygen concentration fields inside and outside the scaffold. The minimum oxygen concentration in the scaffold and its location under different conditions were summarized.

1. Introduction

Scaffolds have been extensively used in tissue engineering [1–5] because they provide a defined, three-dimensional structure for cell attachment and tissue organization [6]. The scaffold structure is expected to have a high porosity for cell–scaffold interaction, cell proliferation and extracellular matrix regeneration, and a high permeability for the purpose of transporting nutrients and metabolites to and from the cells. The bioreactors should provide suitable environment which includes efficient nutrient delivery, waste removal, and mechanical stimulation.

There have been a few studies of flow around scaffolds in bioreactors, in which the scaffold was assumed as a solid body to study its effect on the flow environment. Dusting et al. [7] experimentally investigated, using particle image velocimetry technique, the flow field and shear stress outside a scaffold in a spinner-flask bioreactor. It was found that vortex breakdown may still occur and relatively large stresses occur along the edge of scaffold protruding into the boundary of the vortex breakdown region. Williams et al. [8] developed a FLUENT model to calculate flow fields, shear stresses and oxygen profiles around tissue-engineering constructs, also with the assumption of impermeable constructs, in a concentric cylinder bioreactor. The oxygen distribution in the bioreactor showed that oxygen transport from the fluid-phase to the cartilage constructs was uniform.

There are also a few numerical studies which consider the porous flow through scaffolds. Porter et al. [9] applied the lattice-Boltzmann method to simulate the culture media flowing through scaffolds in a bioreactor. Microcomputed tomography imaging was used to define the micro-architecture of the scaffold for the simulations. The local shear stress was estimated from velocity derivatives at various media flow rates. Boschetti et al. [10] developed a computational fluid dynamic model of the flow though a three-dimensional scaffold of homogeneous geometry. The scaffold was idealized as composing of many sub-units which were obtained by subtracting a solid sphere from a concentric solid cube. In both of the above two approaches, a large number of elements are needed to describe the micro-structure of the scaffolds.

Moving away from the approach based on the scaffold microstructure, Sucosky et al. [11] investigated the flow and shear stress around and through tissue-engineering scaffolds in a spinner-flask bioreactor agitated by a magnetic stir bar. However, the scaffolds were initially assumed as solid structures to calculate the flow and pressure field around them using the commercial software FLUENT. Using these flow and pressure field, the Darcy's law was applied to predict the flow of culture medium through the scaffolds.

The flow in bioreactors with scaffold should be defined as a system which composes of regions of porous media and homogenous fluid. Several numerical methods have been proposed to simulate such type of flow systems. Assuming continuity of both velocity and stress at the porous–fluid interface, Costa et al. [12] proposed a control-volume finite element method to simulate the problems

* Corresponding author.
E-mail address: mpeyp@nus.edu.sg (P. Yu).

0017-9310/$ - see front matter © 2008 Elsevier Ltd. All rights reserved.
doi:10.1016/j.ijheatmasstransfer.2008.06.021

Nomenclature

C	Concentration
C_0	Reference concentration
C^*	Equilibrium weighted average concentration in scaffold
C_F	Forchheimer coefficient
Da	Damkohler number = $\gamma V_m R^2/(C_0 D_f)$
Dar	Darcy number = K/R^2
D_c	Diffusivity of oxygen in animal cell phase
D_{eff}	Effective diffusivity of oxygen in scaffold
D_f	Binary diffusivity
Fr	Froude number = $\Omega^2 R^2/(gH)$
g	gravitational constant (= 9.81 m/s^2)
H	Height
H/R	Aspect ratio
k_m	Half-saturation parameter
K	Permeability
K_{eq}	Partition coefficient
p	Pressure
r, z, θ	Cylindrical coordinates
R	Radius
Re	Reynolds number
u_t	Velocity component parallel to the interface
u_n	Velocity component normal to the interface
$\vec{v}_{interface}$	Interface velocity vector
v_z, v_r, v_θ	Velocity components in cylindrical coordinates
V_m	Maximum oxygen uptake rate per cell

Greek symbols

β_1, β_2	Adjustable parameters for stress jump condition
γ	Cell density
ε	Porosity
ε_c	Volume fractions occupied by animal cells
ε_s	Volume fractions occupied by the scaffold
ν	Kinematic viscosity
ρ	Density of the fluid
Ω	Angular velocity

Superscripts

*	Intrinsic average

of coupled viscous and porous flows. Betchen et al. [13] developed a finite volume model, also based on continuity of both velocity and stress at the interface, but special attention was given to the pressure–velocity coupling there. The implementation of the stress jump condition based on Ochoa-Tapia and Whitaker [14,15] can be found in the numerical work of Silva and de Lemos [16]. Yu et al. [17] developed a numerical approach based on the finite volume method with a collocated variable arrangement to treat the stress jump condition given by Ochoa-Tapia and Whitaker [18], which includes both viscous and inertial effects. This method [17] has been extended to simulate the swirling flow in a bioreactor with a scaffold [19].

The objective of this study was to apply numerical simulations to predict the fluid dynamics and oxygen transport inside a micro-bioreactor for animal cell culture. A tissue engineering scaffold was mounted in the bioreactor for cell attachment. Chinese hamster ovary (CHO) cells culture was considered here because it is a popular tool in biological research. The present bioreactor, similar to those of Dusting et al. [7] and Yu et al. [20], consists of an open cylinder chamber filled with culture medium; and the medium mixing is generated by the rotating bottom-wall. Such type of bioreactors has an advantage of providing a favorable cell-culture environment with steady, laminar flow and low shear stress [7]. The tissue engineering scaffold was assumed to be a rigid, homogeneous and isotropic porous medium. The finite volume method based on body-fitted and multi-block grid [17,19] was applied. Based on the numerical results, the effect of the presence of scaffold on the flow and oxygen concentration fields was studied. The effects of the important parameters, such as the Reynolds and Darcy numbers, on flow and oxygen concentration fields inside and outside the scaffold were investigated.

2. Computational methods

2.1. Mathematical model

The micro-bioreactor with a tissue engineering scaffold is shown schematically in Fig. 1a. The scaffold with a concentric hole is coaxially mounted in the bioreactor. All CHO cells are assumed to be uniformly attached to the scaffold and no cells are suspended in the culture medium. The substrate considered here is oxygen as insufficient oxygen supply is one of the limiting factors for cell culture.

The computational domain for the bioreactor with the scaffold is shown in Fig. 1b. The geometry is axisymmetric because the scaffold and the bioreactor are concentric. For a typical application, the height of the bioreactor is 10 mm and the diameter is 20 mm. The thickness of the scaffold is 2 mm and the diameter is 12 mm. The diameter of the hole is 3 mm. The scaffold is fixed at the 60% height of the bioreactor.

The porous medium was assumed to consist of the scaffold structure and cells attached on the scaffold, with volume fractions ε_s and ε_c occupied by the scaffold and cells, respectively. The porosity of the porous medium ε, which is the void fraction occupied by the culture medium, can be calculated as:

$$\varepsilon = 1 - (\varepsilon_s + \varepsilon_c) \tag{1}$$

Generally, for the scaffold without cells, the porosity may vary from 0.6–0.95 [2,21]. The permeability of the scaffold is in the range of 10^{-12} to 10^{-9} m^2 [22,23]. However, when cells are attached to the scaffold, the porosity and permeability may change with the cell proliferation. During the process of cell culture, the porosity may drop from 0.92 to 0.73 and the permeability may decrease to 10% of the initial value [24].

The porous medium is considered to be rigid, homogeneous and isotropic, and saturated with the culture medium. Considering the culture medium as a Newtonian fluid and oxygen consumption by CHO cells to be based on Michaelis–Menten equation, the governing equations for the flow and oxygen transport [25–27] can be written as given below.

For homogenous fluid region:

$$\frac{1}{r}\frac{\partial(rv_r)}{\partial r} + \frac{\partial v_z}{\partial z} = 0 \tag{2}$$

$$\frac{1}{r}\frac{\partial(rv_r v_z)}{\partial r} + \frac{\partial(v_z v_z)}{\partial z} = -\frac{1}{\rho}\frac{\partial p}{\partial z} + \nu\left[\frac{1}{r}\frac{\partial}{\partial r}\left(r\frac{\partial v_z}{\partial r}\right) + \frac{\partial^2 v_z}{\partial z^2}\right] \tag{3}$$

$$\frac{1}{r}\frac{\partial(rv_r v_r)}{\partial r} + \frac{\partial(v_z v_r)}{\partial z} = -\frac{1}{\rho}\frac{\partial p}{\partial r} + \nu\left[\frac{\partial}{\partial r}\left(\frac{1}{r}\frac{\partial}{\partial r}(rv_r)\right) + \frac{\partial^2 v_r}{\partial z^2}\right] + \frac{v_\theta^2}{r} \tag{4}$$

$$\frac{1}{r}\frac{\partial(rv_r v_\theta)}{\partial r} + \frac{\partial(v_z v_\theta)}{\partial z} = \nu\left[\frac{\partial}{\partial r}\left(\frac{1}{r}\frac{\partial}{\partial r}(rv_\theta)\right) + \frac{\partial^2 v_\theta}{\partial z^2}\right] - \frac{v_r v_\theta}{r} \tag{5}$$

$$\frac{1}{r}\frac{\partial(rv_r C)}{\partial r} + \frac{\partial(v_z C)}{\partial z} = D_f \nabla^2 C \tag{6}$$

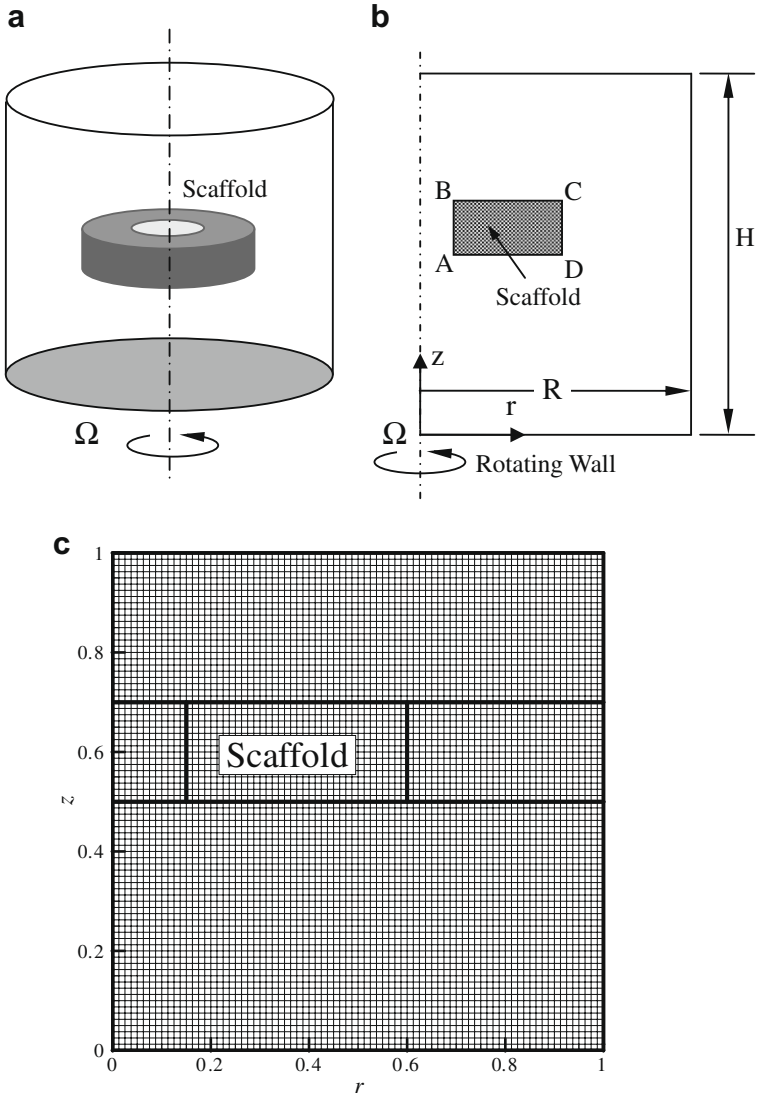

Fig. 1. Micro-bioreactor system with a tissue engineering scaffold; (a) Schematic; (b) computational domain (c) grid topology and domain partitioning, a big grid size was chosen to demonstrate the grid topology clearly.

For porous medium region:

$$\frac{1}{r}\frac{\partial(rv_r)}{\partial r}+\frac{\partial v_z}{\partial z}=0 \tag{7}$$

$$\frac{1}{r}\frac{\partial}{\partial r}\left(\frac{rv_rv_z}{\varepsilon}\right)+\frac{\partial}{\partial z}\left(\frac{v_zv_z}{\varepsilon}\right)=-\frac{1}{\rho}\frac{\partial(\varepsilon p^*)}{\partial z}+\nu\left[\frac{1}{r}\frac{\partial}{\partial r}\left(r\frac{\partial v_z}{\partial r}\right)+\frac{\partial^2 v_z}{\partial z^2}\right]-\frac{\varepsilon v_rv_z}{r}-\frac{\nu\varepsilon}{K}v_z-\frac{\varepsilon C_F\sqrt{v_z^2+v_r^2+v_\theta^2}}{\sqrt{K}}v_z \tag{8}$$

$$\frac{1}{r}\frac{\partial}{\partial r}\left(\frac{rv_rv_r}{\varepsilon}\right)+\frac{\partial}{\partial z}\left(\frac{v_zv_r}{\varepsilon}\right)=-\frac{1}{\rho}\frac{\partial(\varepsilon p^*)}{\partial r}+\nu\left[\frac{\partial}{\partial r}\left(\frac{1}{r}\frac{\partial}{\partial r}(rv_r)\right)+\frac{\partial^2 v_r}{\partial z^2}\right]+\frac{\varepsilon v_\theta^2}{r}-\frac{\nu\varepsilon}{K}v_r-\frac{\varepsilon C_F\sqrt{v_z^2+v_r^2+v_\theta^2}}{\sqrt{K}}v_r \tag{9}$$

$$\frac{1}{r}\frac{\partial}{\partial r}\left(\frac{rv_rv_\theta}{\varepsilon}\right)+\frac{\partial}{\partial z}\left(\frac{v_zv_\theta}{\varepsilon}\right)=\nu\left[\frac{\partial}{\partial r}\left(\frac{1}{r}\frac{\partial}{\partial r}(rv_\theta)\right)+\frac{\partial^2 v_\theta}{\partial z^2}\right]-\frac{\varepsilon v_rv_\theta}{r}-\frac{\nu\varepsilon}{K}v_\theta-\frac{\varepsilon C_F\sqrt{v_z^2+v_r^2+v_\theta^2}}{\sqrt{K}}v_\theta \tag{10}$$

$$\frac{1}{r}\frac{\partial(rv_rC^*)}{\partial r}+\frac{\partial(v_zC^*)}{\partial z}=D_{\text{eff}}\nabla^2C^*-\gamma V_m\frac{K_{eq}C^*}{K_{eq}C^*+k_m} \tag{11}$$

where C is the concentration in homogenous fluid region; C^* is the equilibrium weighted average concentration in porous medium region [26]; K_{eq} is the partition coefficient and set to 1 [27] currently; D_{eff} is the effective diffusivity of oxygen in the porous medium, and its value is determined by the Maxwell's equation [27,28] in this study. However, the Maxwell's equation neglects the resistance for mass transfer across the cell membrane. If this resistance has to be considered, D_{eff} can be approximated by the Chang's unit cell model [28,29].

Note that Eq. (11) starts from a boundary value problem of diffusion–convection and reaction in cell culture systems. The diffusion–convection equation is applied to describe nutrient transport in culture medium. The scaffold is considered as a rigid impermeable phase, while animal cells are considered as a continuum. The physical model used in the cell phase to describe reaction and mass transport is a single diffusion-reaction equation. The set of microscopic equations governing transport phenomena in the culture systems is averaged in a representative elementary volume, which is much larger than the pore scale and considerably smaller than the macroscopic flow domain, to form a macroscopic, one-equation model to describe the nutrient transport by diffusion and convection. A complete

derivation of Eq. (11) has been addressed in details in the work by Lasseux et al. [26].

The length and velocity components were scaled by $1/R$ and $1/(\Omega R)$, respectively. The Reynolds number is defined as $Re = \Omega R^2/\nu$ and kept within 2000 to ensure steady flow condition. The Darcy number is defined as $Dar = K/R^2$ and the range of Dar varies from 10^{-7} to 10^{-5}. The Damkohler number is defined as $Da = \gamma V_m R^2/(C_0 D_f)$. The aspect ratio of the bioreactor is fixed at $H/R = 1.0$.

The effective Reynolds number for the flow around the porous scaffold is small although the present Reynolds number based on the rotating bottom-wall is up to 2000. The effective reference length scale for the scaffold is about half of the bioreactor radius. The velocity components in r–z plane at the upper region of the bioreactor without the scaffold are less than 1/20 of the swirling velocity ΩR. Therefore, the effective Reynolds number for the flow around the scaffold is less than 40 even though the Reynolds number based on the rotating bottom-wall is up to 2000.

2.2. Boundary conditions

To solve Eqs. (2)–(11), the appropriate boundary conditions have to be imposed at the interface between the homogenous fluid and porous medium regions. The mass conservation requires the continuities of velocity components at the interface, which can be expressed as:

$$v_r|_{\text{fluid}} = v_r|_{\text{porous}} = v_r|_{\text{interface}} \tag{12}$$

$$v_z|_{\text{fluid}} = v_z|_{\text{porous}} = v_z|_{\text{interface}} \tag{13}$$

$$v_\theta|_{\text{fluid}} = v_\theta|_{\text{porous}} = v_\theta|_{\text{interface}} \tag{14}$$

The continuity of the normal stress can be written as:

$$\left.\frac{\mu}{\varepsilon}\frac{\partial v_n}{\partial n}\right|_{\text{porous}} - \left.\mu\frac{\partial v_n}{\partial n}\right|_{\text{fluid}} = 0 \tag{15}$$

where v_n is the velocity component perpendicular to the interface. Based on the non-local form of the volume-averaged momentum equation, the shear-jump condition, which includes both viscous and inertial jump parameters β_1 and β_2, can be expressed as [18]:

$$\left.\frac{\mu}{\varepsilon}\frac{\partial v_t}{\partial n}\right|_{\text{porous}} - \left.\mu\frac{\partial v_t}{\partial n}\right|_{\text{fluid}} = \beta_1\left.\frac{\mu}{\sqrt{K}}v_t\right|_{\text{interface}} + \beta_2\rho v_t^2|_{\text{interface}} \tag{16}$$

where n is the unit vector normal to the interface; v_t is the velocity component parallel to the interface; β_1 and β_2 are adjustable parameters which account for the stress jump at the interface. Ochoa-Tapia and Whitaker [18] stated that the parameters β_1 and β_2 are dependent on permeability and porosity and found that these two parameters are both of order one. Unfortunately, the values of these parameters for different porous media need to be determined experimentally. However, the effects of the jump parameters β_1 and β_2 on the mass transport are generally small [30]. Thus β_1

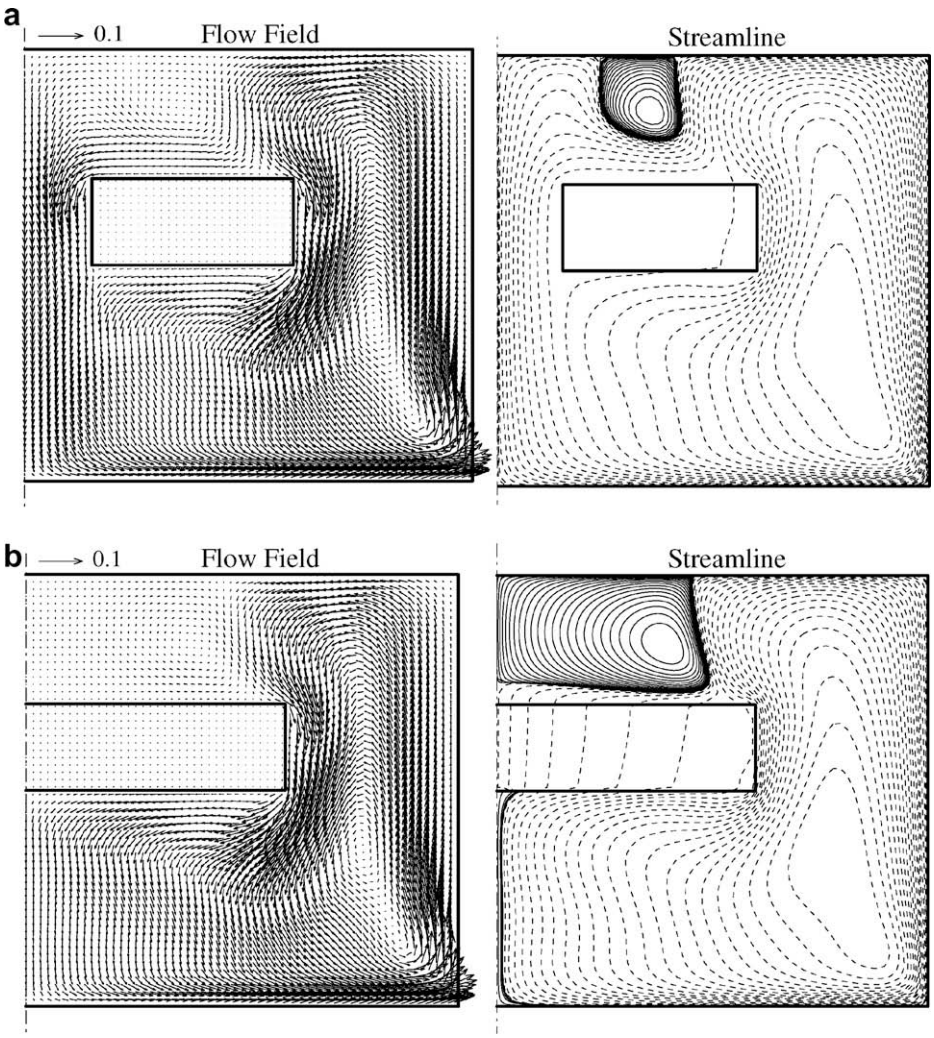

Fig. 2. Flow field and streamlines in the bioreactor; (a) scaffold with concentric hole; (b) scaffold without the concentric hole; $H/R = 1$, $Re = 1500$, $Dar = 5 \times 10^{-6}$, $\varepsilon = 0.6$. Contour levels C_i are non-uniformly spaced, with 25 positive levels $C_i = \text{Max(variable)} \times (i/25)^4$ and 25 negative levels $C_i = \text{Min(variable)} \times (i/25)^4$.

and β_2 were fixed at 0.7 and 0 in this study unless specified otherwise.

As for the oxygen transport, considering a steady-state condition and based on the non-local form of the volume-averaged mass transport equation, the interface boundary conditions [31] can be written as:

$$\varepsilon D_{\mathrm{eff}} \left.\frac{\partial C^*}{\partial n}\right|_{\mathrm{porous}} - D_{\mathrm{f}} \left.\frac{\partial C}{\partial n}\right|_{\mathrm{fluid}} = 0 \tag{17}$$

$$C|_{\mathrm{fluid}} = C^*|_{\mathrm{porous}} = C|_{\mathrm{interface}} \tag{18}$$

For the velocity, the non-slip boundary condition was imposed on the solid wall. The deformation of the free surface due to the rotation of the fluid is proportional to the Froude number *Fr*. As the Reynolds number is less than 2000, *Fr* is negligibly small (in the order of 10^{-3}). Thus, the free surface can be simplified as a flat stress-free surface. For the oxygen transfer, the zero flux conditions were imposed for both side-wall and bottom-wall. The oxygen concentration at the free surface was assumed to be constant and equal to the saturation concentration C_0 in the culture media as determined from Henry's law.

To solve the above equations, a finite volume method with a collocated variable arrangement was used. The multi-block grid method proposed by Lilek et al. [32] was applied. Note that the present numerical method has been successfully applied for both swirling flow problems [33,34] and the coupled problems involving both porous medium and homogenous fluid regions [17,19]. An outline of the present method is given in the Appendix.

An example of the grid topology and domain partitioning is presented in Fig. 1c. The preliminary numerical tests with three different mesh sizes of 1/100, 1/200 and 1/400 (scaled by the radius of micro-bioreactor *R*) confirmed that the solutions based on mesh size of 1/200 are grid-independent. Thus, the present numerical simulations were carried out based on a dimensionless mesh size of 1/200.

3. Results and discussion

3.1. Flow pattern

Fig. 2a presents the typical flow field and streamlines in the bioreactor with the scaffold. The rotating bottom-wall imparts angular momentum to the fluid just above it and centrifuges the fluid towards the side-wall. The fluid then spirals up along the side-wall. Near the free surface, the fluid converges towards the center. A vortex breakdown bubble is attached to the free surface. There is a recirculation region at the right hand side, which is compressed by the presence of the scaffold. The scaffold diverts some of the fluid to the axial region. The scaffold also confines the vortex breakdown bubble to a region above it. The fluid approaches the scaffold almost normally, due to the presence of the vortex break-

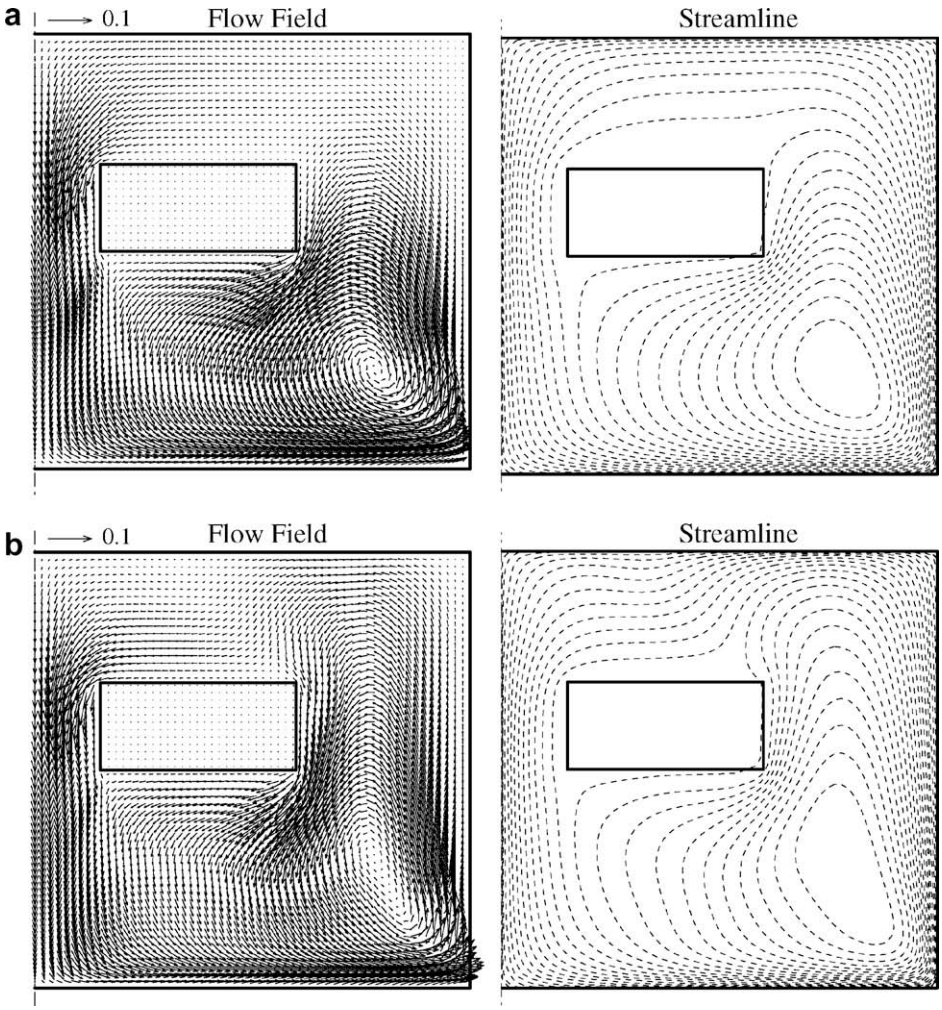

Fig. 3. Flow fields and streamlines in the bioreactor at different *Re*; $H/R = 1$, $Dar = 5 \times 10^{-6}$, $\varepsilon = 0.6$; (a) $Re = 500$; (b) $Re = 1000$. Contour levels C_i are non-uniformly spaced, with 25 positive levels $C_i = \mathrm{Max(variable)} \times (\mathrm{i}/25)^4$ and 25 negative levels $C_i = \mathrm{Min(variable)} \times (\mathrm{i}/25)^4$.

down bubble. There is some porous flow through the scaffold. There is no recirculation region below the scaffold, which is consistent with Dusting et al.'s experiment result [7].

The presence of the scaffold will obstruct the recirculating flow generated by the rotating bottom-wall. If the obstruction is large, regions of flow separation and wake may be formed. Such unfavorable flow patterns are found for a scaffold configuration without the axial hole (see Fig. 2b), in which the axial returning flow is prevented. Only a very small proportion of the fluid passes through the scaffold. A large vortex breakdown bubble is formed above the scaffold. The vortex breakdown bubble hampers flow mixing above the scaffold. Thus it is important that a scaffold configuration does not cause large recirculation bubbles.

The flow field shown above (Fig. 2a) is for $Re = 1500$. Two other Reynolds numbers, 500 and 1000, are considered in Fig. 3. With an increase in Re, the velocity around the top surface of the scaffold becomes higher, which means more fluid is convected to the upper region. The streamline results show that the recirculation region elongates towards the free surface. There are two phenomena associated with the change of Re, due to the formation of a vortex breakdown bubble near the top surface. At a low Re, the flow moves towards the scaffold more obliquely than that at a high Re (compare Figs. 2 and 3a). On the other hand, the flow divides at different locations on the scaffold surface at different Re. The flow divides at the top right hand corner of the scaffold at a low Re (Fig. 3a). However, at a high Re the dividing point has moved to the top surface (Fig. 2a).

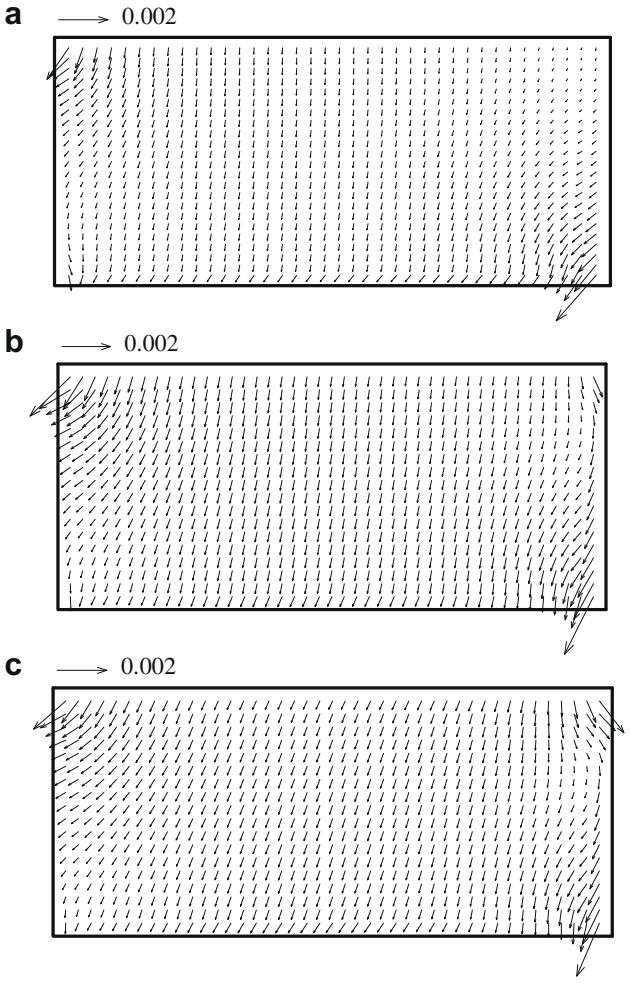

Fig. 4. Flow fields within the scaffold in the bioreactor at different Re; $H/R = s1$, $Dar = 5 \times 10^{-6}$, $\varepsilon = 0.6$; (a) $Re = 500$; (b) $Re = 1000$; (c) $Re = 1500$.

It is seen that there is a vortex breakdown bubble at $Re = 1500$ (Fig. 2a). However, the results for other Re (data not shown) indicate that the onset of vortex breakdown is between $Re = 1000$ and 1200. This critical Re for the onset of vortex breakdown is higher than that (Re around 500) in the bioreactor without the scaffold i.e. the open chamber with end-wall rotating [35]. The size of the vortex breakdown bubble is also smaller. The presence of the scaffold seems to hamper the formation of a vortex breakdown bubble.

The porous flow within the scaffold is shown enlarged in Fig. 4 at different Re. Generally, the flow enters the scaffold from the top and right surfaces and exits from the bottom and left surfaces. The porous flow pattern is related to the external flow pattern. Although the porous flow is dominant in the axial direction (from top to bottom), there are noticeable radial velocity components at the corner regions, mainly due to the external corner flow. At the corner, the external flow changes direction and has a higher radial component, which causes noticeable porous flow in the radial direction.

By comparing Fig. 4a, b, and c, it is noted that there is more porous flow at higher Re. However, the increase is not much at $Re = 1500$. The porous flows at the left and right corners are higher at $Re = 1000$ due to the external flow approaching the scaffold less obliquely than that at $Re = 500$. However, at $Re = 1500$, only the porous flow at the right corner increases noticeably compared with that at $Re = 1000$. This is attributed to the formation of the vortex breakdown bubble which has diverted some of the external flow to the right side. The porous flow at this high $Re = 1500$ also has a relatively larger radial velocity component towards the left hand side, and this is attributed to the larger interface velocity at the top surface (Fig. 2a) arising from the presence of the nearby vortex breakdown bubble.

To show the effect of the permeability, an extreme case, that is the flow around an impermeable scaffold, was simulated with $Re = 1500$. It is found that the flow field around the impermeable scaffold (Fig. 5) does not differ greatly from that of the permeable scaffold (Fig. 2a). The flow field is dominated by the vortex breakdown bubble and recirculation region which appear to be around the same size for various cases. The swirling flow behaviour, in particular the vortex breakdown phenomenon, seems to be mainly influenced by the chamber aspect ratio, the Reynolds number, the scaffold configuration and the scaffold location. The effect of the permeability or porosity is secondary for the present range of parameters.

Fig. 6 shows the effect of Dar on the porous flow within the scaffolds. It is seen that the porous velocity is noticeably higher at a higher Dar (see also Fig. 4c). This is expected because a higher Darcy number means more porous flow for a certain pressure drop. The porosity has a negligible effect on the flow field within the scaffold. The scaffold permeability is the primary factor which determines the porous flow in it.

3.2. Oxygen concentration

The concentrations are presented in the form of the equilibrium weighted average [26] and non-dimensionalized by the saturated concentration C_0 at the free surface. Fig. 7a shows the oxygen concentration field in the bioreactor. The oxygen source is above the free surface which is assumed to be at saturated value. By comparing Figs. 7 and 2a, it is seen that the concentration contours are generally similar to the streamline contours. Near the axial region, oxygen from the free surface is convected downwards to the bottom. Along the rotating bottom-wall, oxygen moves within a thin boundary layer to the side-wall and then up along the wall to the surface. The concentrations in the narrow core at the axis and the thin boundary layers along the walls are high because they are not spread over a large region; moreover, they are not

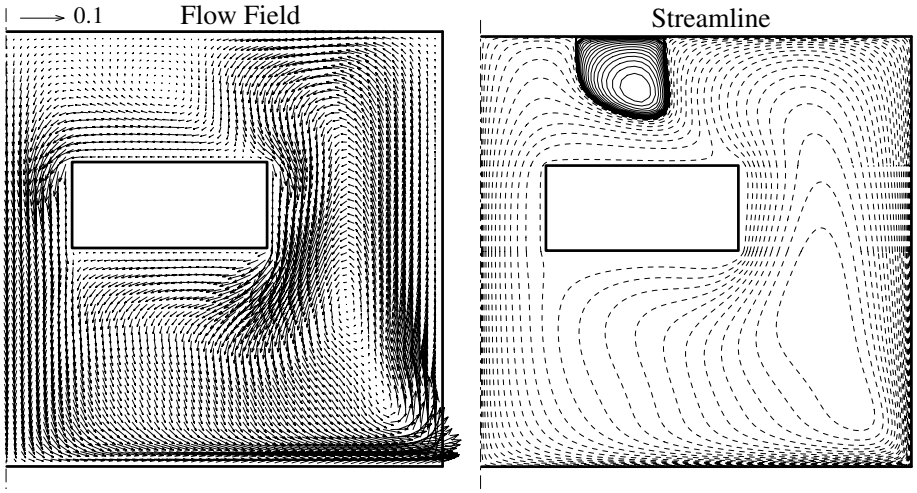

Fig. 5. Flow fields and streamlines in the bioreactor with the impermeable scaffold; $H/R = 1$, $Re = 1500$. Contour levels C_i are non-uniformly spaced, with 25 positive levels $C_i = \text{Max(variable)} \times (\text{i}/25)^4$ and 25 negative levels $C_i = \text{Min(variable)} \times (\text{i}/25)^4$.

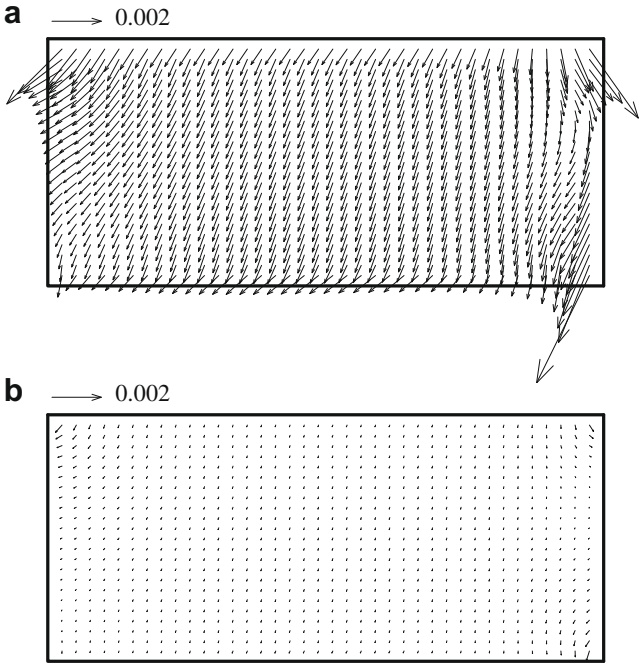

Fig. 6. Flow fields within the scaffold for different *Dar*; $H/R = 1$, $Re = 1500$, $\varepsilon = 0.6$; (a) $Dar = 1 \times 10^{-5}$; (b) $Dar = 1 \times 10^{-6}$.

consumed by any cells. Near the top axial region there is also a high concentration region, where oxygen from the free surface is recirculated within the vortex breakdown bubble.

At the top region near the side-wall, oxygen is transported from the free surface and convected downwards by the recirculating flow. Some of the downward flow convects oxygen to the scaffold. Note that the oxygen convection to the scaffold is mainly from this region to the right of the vortex breakdown bubble. The axial region and the vortex breakdown region play a small role in convecting oxygen to the scaffold. The concentration in the main recirculation region is about 15% below the saturated concentration, which is not as high as that at the axis region. This indicates that the mixing in the bioreactor may be satisfactory. The concentration around the scaffold is satisfactory despite the minimal role of the axial region and the vortex breakdown bubble in oxygen transport.

The concentration in the scaffold is around 40% lower than that in the surrounding medium. The concentration is higher at the top and right surfaces and lower near the bottom surface of the scaffold. The concentration inside the scaffold reduces due to the consumption by the cells inside. The concentration contours are influenced by the general direction of the porous flow. The medium enters from the top and right surfaces and exits from the left and bottom surfaces, which is consistent with the concentration contours. The concentration falls as the medium passes through the scaffold, because oxygen is being consumed by the cells. When the low-oxygen medium exits from the bottom surface, it radially converges towards the left bottom edge. From that corner, a streak of low-oxygen fluid spirals downwards.

Fig. 7b shows the oxygen concentration distribution in the bioreactor without any medium circulation ($Re = 0$). It is seen that without flow, the oxygen concentration falls rapidly from its saturation value at the surface to around 10% at the scaffold surface and near zero within the scaffold. This indicates that diffusion alone is not adequate to transfer enough oxygen into the scaffold.

Fig. 8 shows the oxygen concentration distributions within the scaffold at different medium circulation ($Re = 500$ and 1500). With recirculating flow generated by the bottom-wall rotation, there is more oxygen convection to the scaffold surface. At a high *Re*, the concentration within the scaffold is above 80% of saturation but at a small *Re* it is below 20%.

The concentration within the scaffold could reach a low value especially at a small *Re* (Fig. 8a). It is important to make sure that the minimum value does not fall below the critical value to avoid hypoxia. Fig. 9a summarizes the variation of the minimum oxygen concentrations within the scaffold with *Re*. It is seen that the minimum concentrations increase rapidly with an increase in *Re* (Fig. 9a). At a low $Re = 500$, it is below that the critical value of 5% of saturation for CHO cell culture [36]. Thus, the micro-bioreactor should be operated at *Re* above 500. However, to have an optimal concentration around 50% of saturation [37], the Reynolds number should be around 1000.

Fig. 9b shows the locations of the minimum oxygen concentration in the scaffold at different *Re*. With no medium circulation ($Re = 0$) the location of the minimum concentration is around the central region because of oxygen diffusion from the four surfaces of the scaffold. With porous flow, the location of the minimum oxygen concentration moves downwards to the bottom surface. It is around the middle of the bottom surface at moderate *Re* from 500 to 1000. This is because the porous flow is generally from top

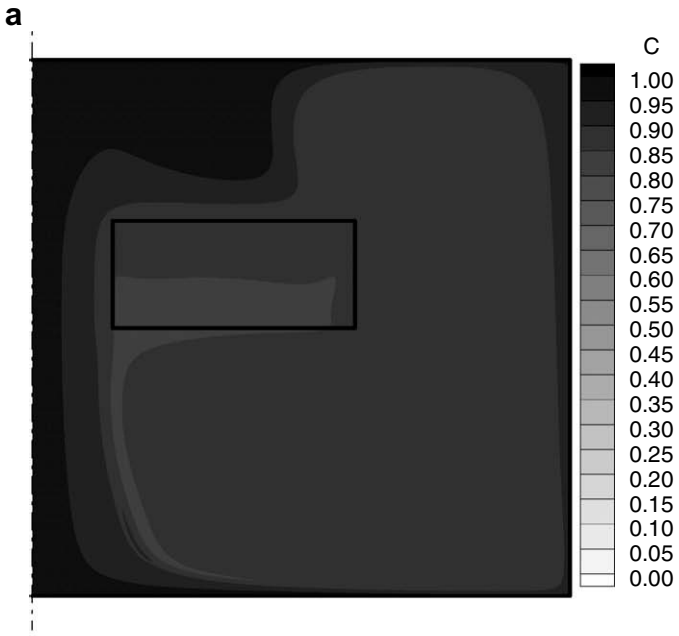

Fig. 7. Oxygen concentration distribution in the bioreactor; (a) $Re = 1500$; (b)$Re = 0$; $H/R = 1$, $Dar = 1 \times 10^{-6}$, $\varepsilon = 0.6$, $Da = 200$.

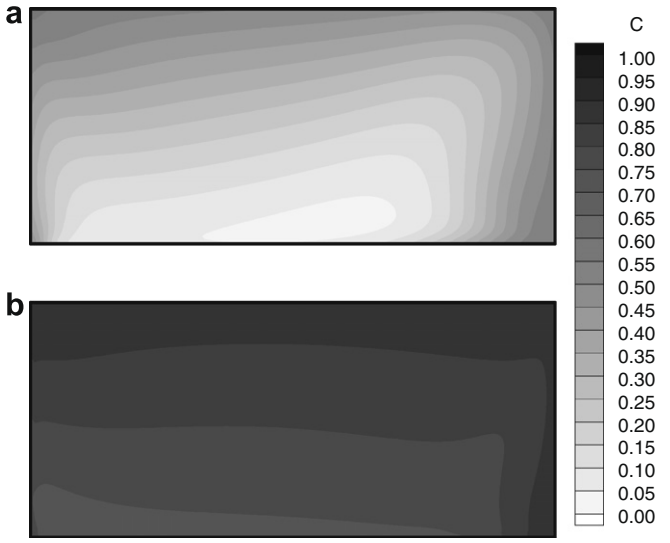

Fig. 8. Oxygen concentration distributions within the scaffold at different *Re*; $H/R = 1$, $Dar = 5 \times 10^{-6}$, $\varepsilon = 0.6$, $Da = 200$; (a) $Re = 500$ and (b) $Re = 1500$.

to bottom surfaces. At a *Re* from 1000 to 2000, the minimum location moves towards the left edge. This is because there is a bigger component of porous flow in the radial direction as discussed above.

Fig. 10 shows the oxygen concentration distributions within the scaffold for different *Dar*. It is seen that, for a low *Dar*, the concentration within the scaffold is low (Fig. 10b). In the central region it is around 50% of its saturation value, and near the bottom it falls to around 25% of saturation. In comparison, the concentration for a high *Dar*of 10^{-5} is above 80% of saturation (Fig. 10a). The porous flow at a small *Dar* is small and thus less oxygen is convected into scaffold, resulting in lower concentration.

Fig. 11a shows the minimum oxygen concentrations within the scaffold at different *Dar*. It is seen that the minimum concentration is very low at small *Dar* due to low porous flow. In fact at *Dar* below 5×10^{-7} it is even below the critical concentration of 5%. To ensure that the concentration is optimal everywhere within the scaffold, the Darcy number should be larger than 1×10^{-6}. Note that this condition is for $Re = 1500$. At a lower *Re*, the concentration will be lower.

Fig. 11b shows the variation in the locations of the minimum oxygen concentrations within the scaffold with *Dar*. At a higher *Dar*, the minimum concentration shifts towards the bottom left corner due to more porous flow. However, the shift is not much as compared to that caused by changing *Re* (Fig. 9b). The shift of minimum location is influenced by porous flow and its direction, on which the Reynolds number has a dominant effect. There is no much difference between the concentration contours for different porosity. The scaffold permeability has an important effect on oxygen concentration distribution in it, and the porosity is of secondary importance.

Fig. 12 shows the oxygen concentration distributions within the scaffold for different *Da*. It is seen that, for a high *Da*=740, the concentration within the scaffold is low (Fig. 12b). In the central region it is around 40% of its saturation value, and near the bottom it falls to around 10% of saturation. In comparison, the concentration for a low $Da = 74$ is above 90% of saturation (Fig. 12a). A higher Damkohler number means a higher oxygen consumption rate. Thus, more oxygen is consumed by the cells, resulting in lower concentration distribution.

Fig. 13 shows the minimum oxygen concentrations within the scaffold at different *Da*. It is seen that the minimum concentration is very low at a high *Da* due to high oxygen consumption rate. In fact at *Da* above 800 it is even below the critical concentration (5% of saturation). To ensure that the concentration is optimal (around 50% of saturation) everywhere within the scaffold, the Damkohler number should be less than 500. Note that this condition is for $Re = 1500$ and $Dar = 5 \times 10^{-6}$. At a lower *Re* or *Dar*, the concentration will be lower.

During the cell culture, the cell density may increase much because of the proliferation. An increase in the cell density means an increase in *Da*. Thus, the oxygen concentration within the scaffold drops with the cell proliferation. Moreover, when cells are seeded in the scaffold, they occupy void space and change the micro-structure of the porous medium. Thus, the presence of the cells may make the porosity and permeability of the scaffold decrease. As mentioned before, the permeability has an important effect on the porous flow, subsequently the oxygen convection in the scaf-

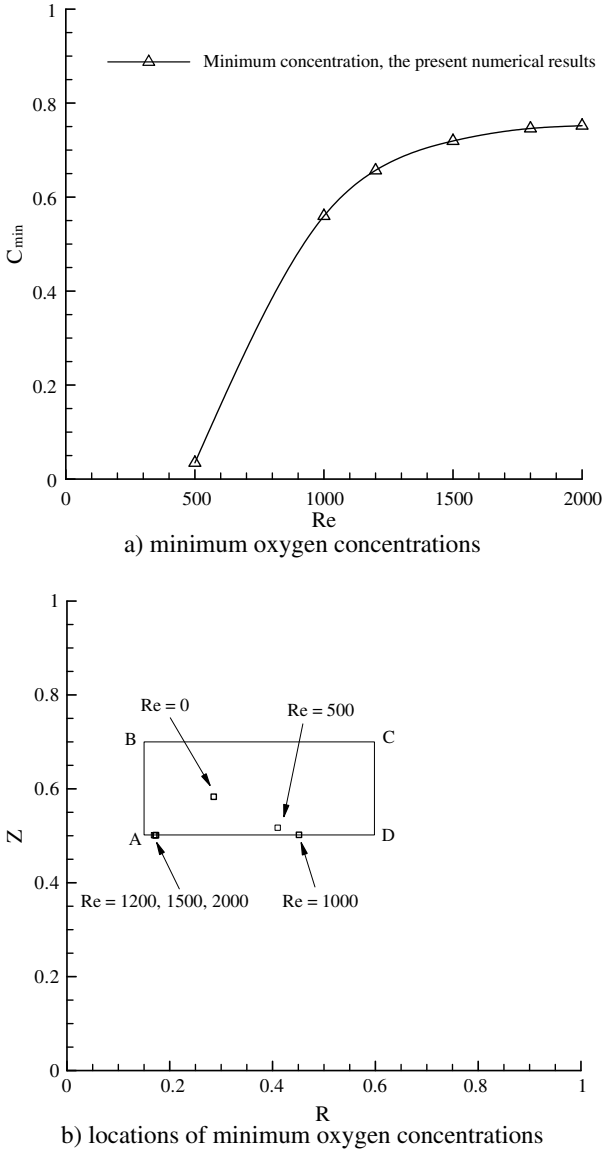

Fig. 9. Variation of the minimum oxygen concentrations and their locations within the scaffold with *Re*; $H/R = 1$, $Dar = 5 \times 10^{-6}$, $\varepsilon = 0.6$, $Da = 200$.

fold. If an increase in the cell density reduces the permeability of the scaffold, the oxygen concentration will suffer an additional drop with the cell proliferation. However, it is very difficult to quantitatively investigate the effect of the cell density on the permeability as it is very difficult to determine the change of the micro-structure of the scaffold when the cells attach and multiply there.

Besides the above dimensionless parameters, there are other parameters that may also affect the concentration distribution in the scaffold. In the above simulations, the jump parameters β_1 and β_2 were fixed at 0.7 and 0. However, the variation of minimum oxygen concentration in the scaffold is less than 1% if β_1 was varied from 0.7 to −0.7. This indicates that the jump parameters have negligible effect on the concentration field, which is similar to the effect of jump parameters on the temperature field or Nusselt number distribution reported by Alazmi and Vafai [30]. Another parameter that needs to be paid attention to is the half-saturation parameter k_m (substrate concentration at which specific uptake rate is half maximal). For cell culture, cell hypoxia is often defined as the condition when the oxygen concentration is less than k_m [38].

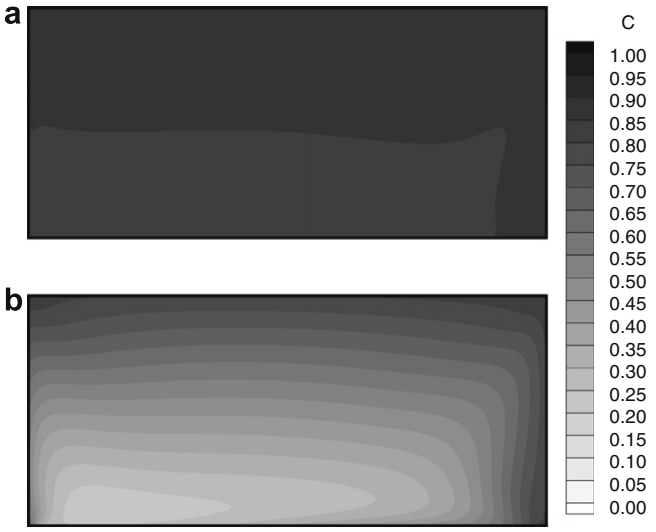

Fig. 10. Oxygen concentration distributions within the scaffold at different *Dar*; $H/R = 1$, $Re = 1500$, $\varepsilon = 0.6$, $Da = 200$; (a) $Dar = 1 \times 10^{-5}$ and (b) $Dar = 1 \times 10^{-6}$.

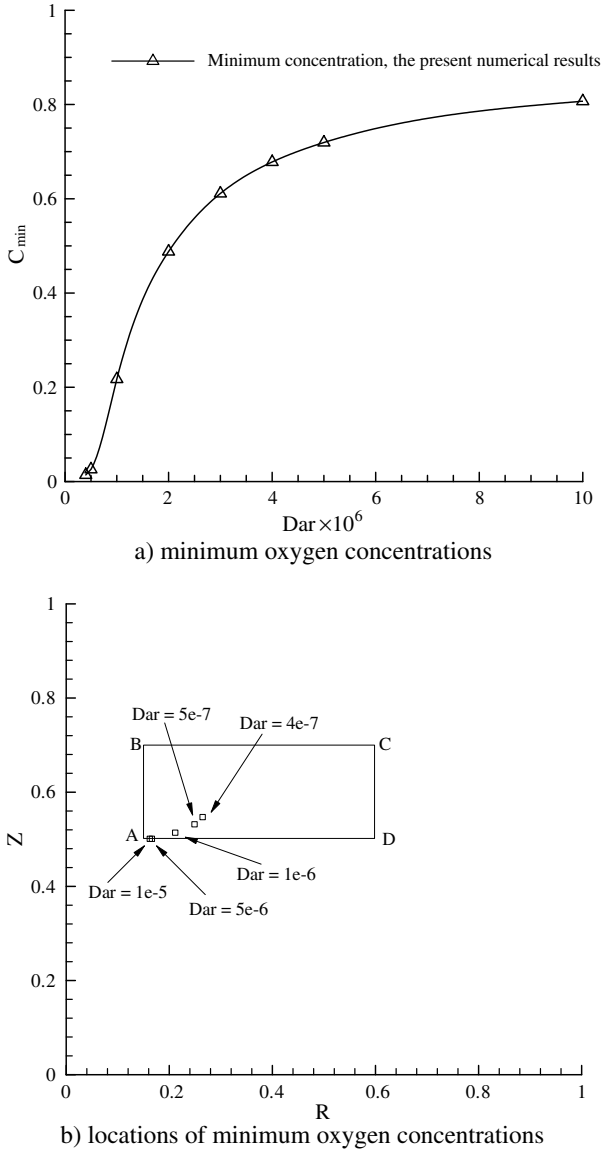

Fig. 11. Variation of the minimum oxygen concentrations and their locations within the scaffold with *Dar*; $H/R = 1$, $Re = 1500$, $\varepsilon = 0.6$, $Da = 200$.

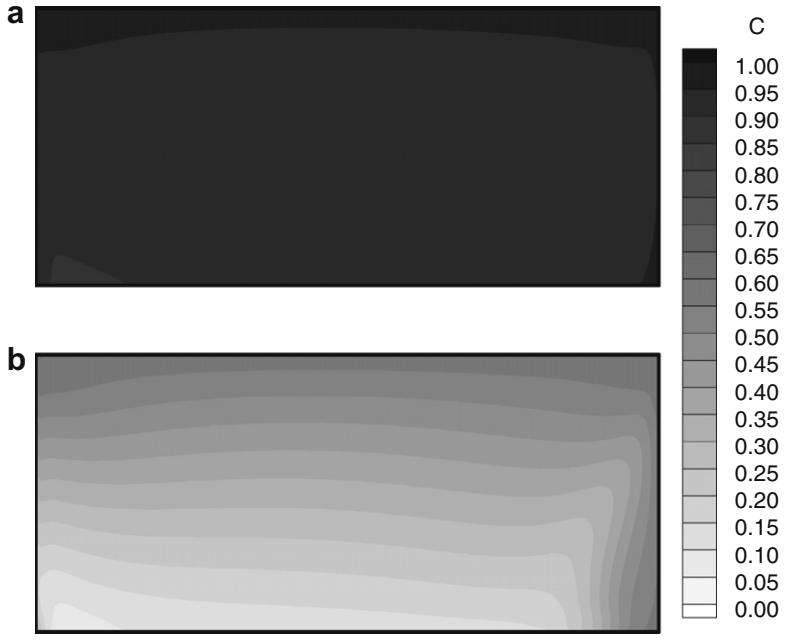

Fig. 12. Oxygen concentration distributions within the scaffold at different *Da*; $H/R = 1$, $Re = 1500$, $Dar = 5 \times 10^{-6}$, $\varepsilon = 0.6$; (a) $Da = 74$ and (b) $Da = 740$.

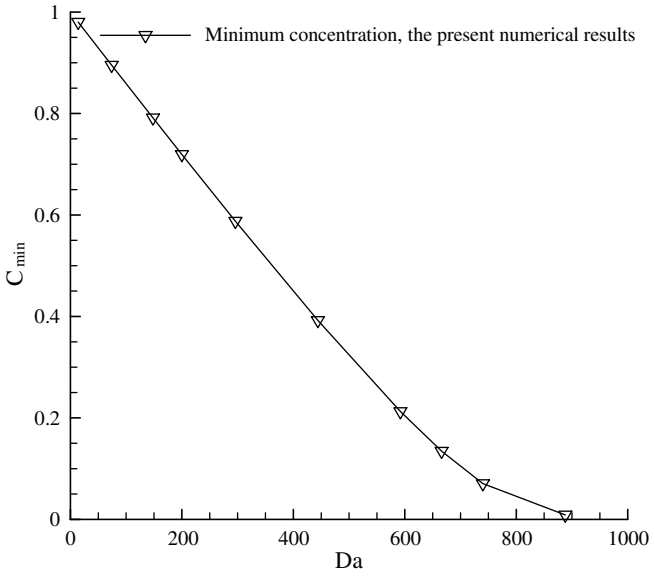

Fig. 13. Variation of the minimum oxygen concentrations within the scaffold with *Da*; $H/R = 1$, $Dar = 5 \times 10^{-6}$, $\varepsilon = 0.6$, $Re = 1500$.

The minimum oxygen concentration in the scaffold increases with k_m. However, compared with other parameters such as *Re* and *Dar*, the effect of k_m on the minimum oxygen concentration is relatively smaller. For the conditions of $Dar = 5 \times 10^{-6}$, $Re = 1500$ and $Da = 200$, the variation of minimum oxygen concentration in the scaffold is less than 5% if the dimensionless k_m (non-dimensionalized by the saturated concentration C_0) was varied from 0 to 0.1.

4. Concluding remarks

In this study, the flow and oxygen concentration fields in a micro-bioreactor with a tissue engineering scaffold were simulated. The medium mixing in the micro-bioreactor was generated by the rotating bottom-wall. The present flow configuration is similar to that of Dusting et al. [7]. However, the scaffold geometry was different in this study which also considered the effects of the porous flow.

It is seen that there is a recirculation region above the bottom-wall. Beyond a certain Reynolds number, a vortex breakdown bubble attached to the free surface is observed. These phenomena are similar to those in the micro-bioreactor without scaffold. However, compared with those in the micro-bioreactor without scaffold, the presence of the scaffold compresses the recirculation region, delays the onset of vortex breakdown and confines the vortex breakdown bubble to a region above the scaffold. There is some porous flow through the scaffold. Generally, the porous flow is dominant in the axial direction (from the top to bottom). Interestingly there is no wake or recirculation region below the scaffold.

The Reynolds number has noticeable effects on the flow fields both outside and inside the scaffold. At a higher Reynolds number, the velocity around the top surface of the scaffold becomes higher and the flow approaches the scaffold more perpendicularly. Also, there is more porous flow within the scaffold with an increase in Reynolds number. The vortex breakdown bubble occurs at Reynolds number above 1200, which causes a relatively larger radial velocity component towards the left hand side within the scaffold.

The flow field outside the scaffold is not affected much by the variation in the permeability or the porosity. However, the porous flow within the scaffold is higher at larger permeability. The general direction of the porous flow has influence on the concentration contours. Generally, the oxygen concentration within the scaffold is higher and the concentration difference between the top and bottom surfaces is lower at a higher Reynolds number or Darcy number.

Also summarized are the minimum oxygen concentrations in the scaffold at different Reynolds numbers, Darcy numbers, and Damkohler numbers, which would benefit the practical cell culture applications.

Appendix

The velocity vector at the interface is given by $\vec{v}_{\text{interface}}$ and can be written as:

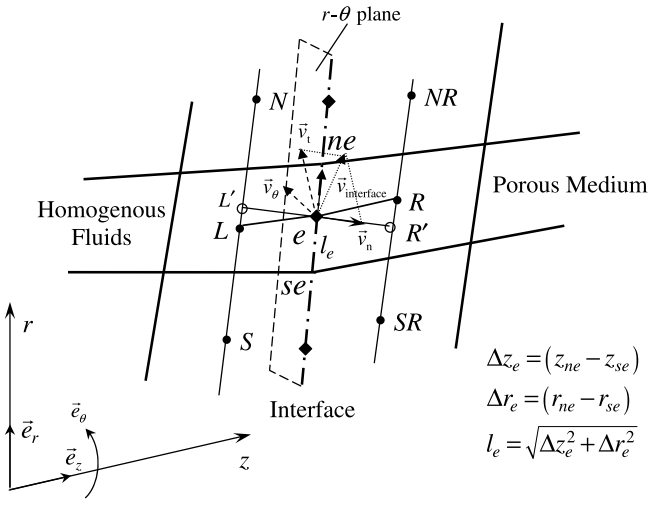

Fig. A1. Interface between two blocks with matching grids.

$$\vec{v}_{\text{interface}} = v_r\vec{e}_r + v_z\vec{e}_z + v_\theta\vec{e}_\theta = v_n\vec{n} + v_t\vec{t} \tag{A1}$$

And the component u_t then can be written as:

$$v_t = (v_r\vec{e}_r + v_z\vec{e}_z + v_\theta\vec{e}_\theta)\cdot\vec{t} \tag{A2}$$

By combining Eqs. (17), (18), and (A2):

$$\frac{\mu}{\varepsilon}\frac{\partial\vec{v}_{\text{interface}}}{\partial n}\bigg|_{\text{porous}} - \mu\frac{\partial\vec{v}_{\text{interface}}}{\partial n}\bigg|_{\text{fluid}} = \beta_1\frac{\mu}{\sqrt{K}}v_t\vec{t} + \beta_2\rho v_t^2\vec{t} \tag{A3}$$

As the flow is axisymmetric, the unit vector ($\vec{t}$) parallel to the interface (Fig. A1) is calculated from:

$$\vec{t} = \left(\frac{v_r\Delta r + v_z\Delta z}{l}\right)\left(\frac{\Delta r\vec{e}_r + \Delta z\vec{e}_z}{l}\right) + v_\theta\vec{e}_\theta\Big/\sqrt{\left(\frac{v_r\Delta r + v_z\Delta z}{l}\right)^2 + v_\theta^2} \tag{A4}$$

By substituting the components of $\vec{v}_{\text{interface}}$ in z, r, and θ directions, the Eq. (A3) becomes:

$$\frac{\mu}{\varepsilon}\frac{\partial v_z}{\partial n}\bigg|_{\text{porous}} - \mu\frac{\partial v_z}{\partial n}\bigg|_{\text{fluid}} = \beta_1\frac{\mu}{\sqrt{K}}\frac{v_z\Delta z\Delta z + v_r\Delta r\Delta z}{l^2} + \beta_2\rho\frac{v_z\Delta z\Delta z + v_r\Delta r\Delta z}{l^2}\sqrt{\left(\frac{v_r\Delta r + v_z\Delta z}{l}\right)^2 + v_\theta^2} \tag{A5}$$

$$\frac{\mu}{\varepsilon}\frac{\partial v_r}{\partial n}\bigg|_{\text{porous}} - \mu\frac{\partial v_r}{\partial n}\bigg|_{\text{fluid}} = \beta_1\frac{\mu}{\sqrt{K}}\frac{v_z\Delta z\Delta r + v_r\Delta r\Delta r}{l^2} + \beta_2\rho\frac{v_z\Delta z\Delta r + v_r\Delta r\Delta r}{l^2}\sqrt{\left(\frac{v_r\Delta r + v_z\Delta z}{l}\right)^2 + v_\theta^2} \tag{A6}$$

$$\frac{\mu}{\varepsilon}\frac{\partial v_\theta}{\partial n}\bigg|_{\text{porous}} - \mu\frac{\partial v_\theta}{\partial n}\bigg|_{\text{fluid}} = \beta_1\frac{\mu}{\sqrt{K}}v_\theta + \beta_2\rho v_\theta\sqrt{\left(\frac{v_r\Delta r + v_z\Delta z}{l}\right)^2 + v_\theta^2} \tag{A7}$$

The derivatives at the interface are calculated from the values at auxiliary nodes L' and R'; these nodes lie at the intersection of the cell face normal n and straight lines connecting nodes L and N or R and NR, respectively, as shown in Fig. A1. The normal gradients at the interface can be calculated by using the first order difference approximation:

$$\frac{\partial v_r}{\partial n}\bigg|_{\text{porous}} = \frac{v_r|_{R'} - v_r|_e}{L_{eR'}},\ \frac{\partial v_z}{\partial n}\bigg|_{\text{porous}} = \frac{v_z|_{R'} - v_z|_e}{L_{eR'}},\ \frac{\partial v_\theta}{\partial n}\bigg|_{\text{porous}} = \frac{v_\theta|_{R'} - v_\theta|_e}{L_{eR'}} \tag{A8}$$

$$\frac{\partial v_r}{\partial n}\bigg|_{\text{fluid}} = \frac{v_r|_e - v_r|_{L'}}{L_{L'e}},\ \frac{\partial v_z}{\partial n}\bigg|_{\text{fluid}} = \frac{v_z|_e - v_z|_{L'}}{L_{L'e}},\ \frac{\partial v_\theta}{\partial n}\bigg|_{\text{fluid}} = \frac{v_\theta|_e - v_\theta|_{L'}}{L_{L'e}} \tag{A9}$$

The velocity components at L' and R' can be calculated by using bilinear interpolation or by using the gradient at the control-volume center:

$$v_r|_{L'} = v_r|_L + (gradv_r)_L\cdot\vec{L'L} \tag{A10}$$

Similarly, the normal gradients of C at the interface can also be calculated by using the first order difference approximation:

$$\frac{\partial C^*}{\partial n}\bigg|_{\text{porous}} = \frac{C^*|_{R'} - C|_e}{L_{eR'}} \tag{A11}$$

$$\frac{\partial C}{\partial n}\bigg|_{\text{fluid}} = \frac{C|_e - C|_{L'}}{L_{L'e}} \tag{A12}$$

The values of C at L' and R' can be calculated by using bilinear interpolation or by using the gradient at the control volume center:

$$C|_{L'} = C|_L + (gradC)_L\cdot\vec{L'L} \tag{A13}$$

References

[1] R.L. Carrier, M. Papadaki, M. Rupnick, F.J. Schoen, N. Bursac, R. Langer, L.E. Freed, G. Vunjak-Novakovic, Cardiac tissue engineering: cell seeding, cultivation parameters and tissue construct characterization, Biotechnol. Bioeng. 64 (1999) 580–589.

[2] J.A. Cooper, H.H. Lu, F.K. Ko, J.W. Freeman, C.T. Laurencin, Fiber-based tissue-engineered scaffold for ligament replacement: design considerations and in vitro evaluation, Biomaterials 26 (2005) 1523–1532.

[3] A.S. Goldstein, T.M. Juarez, C.D. Helmke, M.C. Gustin, A.G. Mikos, Effect of convection on osteoblastic cell growth and function in biodegradable polymer foam scaffolds, Biomaterials 22 (2001) 1279–1288.

[4] C.J. Koh, A. Atala, Tissue engineering, stem cells, and cloning: opportunities for regenerative medicine, J. Am. Soc. Nephrol. 15 (2004) 1113–1125.

[5] G. Vunjak-Novakovic, B. Obradovic, I. Martin, P.M. Bursac, R. Langer, L.E. Freed, Dynamic cell seeding of polymer scaffolds for cartilage tissue engineering, Biotechnol. Prog. 14 (1998) 193–202.

[6] L.E. Freed, G. Vunjak-Novakovic, R.J. Biron, D.B. Eagles, D.C. Lesnoy, S.K. Barlow, R. Langer, Biodegradable polymer scaffolds for tissue engineering, Biotechnology 12 (1994) 689–693.

[7] J. Dusting, J. Sheridan, K. Hourigan, A fluid dynamic approach to bioreactor design for cell and tissue culture, Biotechnol. Bioeng. 94 (2006) 1197–1208.

[8] K.A. Williams, S. Saini, T.M. Wick, Computational fluid dynamics modeling of steady-state momentum and mass transport in a bioreactor for cartilage tissue engineering, Biotechnol. Prog. 18 (2002) 951–963.

[9] B. Porter, P. Zauel, H. Stockman, R. Guldberg, D. Fyhrie, 3-D computational modeling of media flow through scaffolds in a perfusion bioreactor, J. Biomech. 38 (2005) 543–549.

[10] F. Boschetti, M.T. Raimondi, F. Migliavacca, G. Dubini, Prediction of the micro-fluid dynamic environment imposed to three-dimensional engineered cell systems in bioreactors, J. Biomech. 39 (2006) 418–425.

[11] P. Sucosky, F.F. Osorio, J.B. Brown, G.P. Neitzel, Fluid mechanics of a spinner-flask bioreactor, Biotechnol. Bioeng. 85 (2004) 34–46.

[12] V.A.F. Costa, L.A. Oliveira, B.R. Baliga, A.C.M. Sousa, Simulation of coupled flows in adjacent porous and open domains using a control-volume finite-element method, Numer. Heat Tr. A-Appl. 45 (2004) 675–697.

[13] L. Betchen, A.G. Straatman, B.E. Thompson, A nonequilibrium finite-volume model for conjugate fluid/porous/solid domains, Numer. Heat Tr. A-Appl. 49 (2006) 543–565.

[14] J.A. Ochoa-Tapia, S. Whitaker, Momentum transfer at the boundary between a porous medium and a homogeneous fluid I: theoretical development, Int. J. Heat Mass Transfer 38 (1995) 2635–2646.

[15] J.A. Ochoa-Tapia, S. Whitaker, Momentum transfer at the boundary between a porous medium and a homogeneous fluid II: comparison with experiment, Int. J. Heat Mass Transfer 38 (1995) 2647–2655.

[16] R.A. Silva, M.J.S. de Lemos, Numerical analysis of the stress jump interface condition for laminar flow over a porous layer, Numer. Heat Tr. A-Appl. 43 (2003) 603–617.

[17] P. Yu, T.S. Lee, Y. Zeng, H.T. Low, A numerical method for flows in porous and open domains coupled at the interface by stress jump, Int. J. Numer. Meth. Fl. 53 (2007) 1755–1775.

[18] J.A. Ochoa-Tapia, S. Whitaker, Momentum jump condition at the boundary between a porous medium and a homogeneous fluid: inertial effect, J. Porous Media 1 (1998) 201–217.

[19] P. Yu, A Numerical study of swirling flow and oxygen transport in a micro-biorector, Ph.D. Thesis, National University of Singapore, Singapore, 2006.

[20] P. Yu, T.S. Lee, Y. Zeng, H.T. Low, Effect of vortex breakdown on mass transfer in a cell culture bioreactor, Mod. Phys. Lett. B 19 (2005) 543–1546.

[21] Z. Gugala, S. Gogolewski, The in vitro growth and activity of sleep osteoblasts on three-dimensional scaffolds from poly (L/DL-lactide) 80/20%, J. Biomed. Mater. Res. A 75 (2005) 702–709.

[22] S.H. Li, J.R. de Wijn, J.P. Li, P. Layrolle, K. de Groot, Macroporous biphasic calcium phosphate scaffold with high permeability/porosity ratio, Tissue Eng. 9 (2003) 535–548.

[23] S. Wang, J.M. Tarbell Effect of fluid flow on smooth muscle cells in a 3-dimensional collagen gel model, Arterioscler. Thromb. Vasc. Biol. 20 (2000) 2220–2225.

[24] C.M. Agrawal, J.S. McKinney, D. Lanctot, K.A. Athanasiou, Effects of fluid flow on the in vitro degradation kinetics of biodegradable scaffolds for tissue engineering, Biomaterials 21 (2000) 2443–2452.
[25] C.J. Galban, B.R. Locke, Analysis of cell growth kinetics and substrate diffusion in a polymer scaffold, Biotechnol. Bioeng. 65 (1999) 121–132.
[26] D. Lasseux, A. Ahmadi, X. Cleis, J. Garnier, A macroscopic model for species transport during in vitro tissue growth obtained by the volume averaging method, Chem. Eng. Sci. 59 (2004) 1949–1964.
[27] B.D. Wood, S. Whitaker, Multi-species diffusion and reaction in biofilms and cellular media, Chem. Eng. Sci. 55 (2000) 3397–3418.
[28] B.D. Wood, M. Quintard, S. Whitaker, Calculation of effective diffusivities for biofilms and tissues, Biotechnol. Bioeng. 77 (2002) 495–516.
[29] H.C. Chang, Effective diffusion and conduction in two-phase media: a unified approach, AIChE J. 29 (1983) 846–853.
[30] B. Alazmi, K. Vafai, Analysis of fluid flow and heat transfer interfacial conditions between a porous medium and a fluid layer, Int. J. Heat Mass Transfer 44 (2001) 1735–1749.
[31] J.J. Valencia-López, G. Espinosa-Paredes, J.A. Ochoa-Tapia, Mass transfer jump condition at the boundary between a porous medium and a homogeneous fluid, J. Porous Media 6 (2003) 33–49.
[32] Ž. Lilek, S. Muzaferija, M. Perić, V. Seidl, An implicit finite-volume method using nonmatching blocks of structured grid, Numer. Heat Tr. B-Fund. 32 (1997) 385–401.
[33] P. Yu, T.S. Lee, Y. Zeng, H.T. Low, Effects of conical lids on vortex breakdown in an enclosed cylindrical chamber, Phys. Fluids 18 (2006) 117101.
[34] P. Yu, T.S. Lee, Y. Zeng, H.T. Low, Characterization of flow behavior in an enclosed cylinder with a partially rotating end-wall, Phys. Fluids 19 (2007) 057104.
[35] A. Spohn, M. Mory, E.J. Hopfinger, Observation of vortex breakdown in an open cylindrical container with a rotating bottom, Exp. Fluids 14 (1993) 70–77.
[36] A.A. Lin, W.M. Miller, CHO cell responses to low oxygen: regulation of oxygen consumption and sensitization to oxidative stress, Biotechnol. Bioeng. 40 (1992) 505–516.
[37] F. Meuwly, F. Loviat, P.A. Ruffieux, A.R. Bernard, A. Kadouri, U. von Stockar, Oxygen supply for CHO cells immobilized on a packed-bed of Fibra-Cel® disks, Biotechnol. Bioeng. 93 (2006) 791–800.
[38] Y. Zeng, T.S. Lee, P. Yu, P. Roy, H.T. Low, Mass transport and shear stress in a microchannel bioreactor: numerical simulation and dynamic similarity, ASME J. Biomech. Eng. 128 (2006) 185–193.